

# Functionalization of Nanostructured TiO<sub>2</sub> Surfaces with Electrodeposited Strontium Doped Calcium Phosphate and Evaluation of BSA Adsorption for Dental Implant Design

Issa S<sup>2\*</sup>, Azevedo C<sup>2</sup>, Pires R<sup>1</sup>, Cenedese P<sup>1</sup> and Dubot P<sup>1</sup>

<sup>1</sup>Institute of Chemistry and Materials Paris-Est, ICMPE-CNRS, 2-8, rue Henri Dunant, 94320 Thiais, France

<sup>2</sup>University Paris Diderot-Paris 7, U.F.R. Odontologie, 5, rue Garancière 75006, Paris, France

## Abstract

The aim of this work is to study the initial adsorption steps of strontium doped calcium phosphate compounds onto a nanostructured TiO<sub>2</sub> surface and to evaluate its influence on the adsorption of Bovine Serum Albumin (BSA). TiO<sub>2</sub> nanotubes (nT-TiO<sub>2</sub>) arrays were fabricated by anodic oxidation of titanium samples in a fluoride-based solution. Calcium phosphate (CaP) and Strontium doped calcium phosphate (Sr.CaP) have been deposited using pulsed electrodeposition process. Surface nanostructuring (nT-TiO<sub>2</sub>) allows the creation of specific reactive sites on TiO<sub>2</sub> surfaces which are not existed on non-nanostructured ones. Scanning Electron Microscopy (SEM) reveals that the most reactive sites on these nanostructured surfaces for CaP adsorption were the nanotube edges where the CaP deposits mostly growth. Due its positive bioactive properties in inducing bone formation on Ti alloys implants, partial substitution of Ca<sup>2+</sup> by Sr<sup>2+</sup> was studied. Results obtained by X-Ray Photoemission Spectroscopy (XPS) and Infrared Spectroscopy (IR) in reflection-absorption mode revealed that for pure CaP coating, the deposited CaP phase was amorphous apatite-like compound (ACP). In the case of Sr<sup>2+</sup> doped CaP, we observed the formation of a more ordered Ca<sub>1-x</sub>Sr<sub>x</sub>HPO<sub>4</sub> compound similar to Dicalcium Phosphate Anhydrous (DCPA; CaHPO<sub>4</sub>) or Dicalcium phosphate dihydrate (DCPD; CaHPO<sub>4</sub>·2H<sub>2</sub>O) which is more resorbable than ACP or hydroxyapatite (HAP).

BSA adsorption on these functionalized surfaces has been realized at neutral, acidic and basic pH values. Kinetic and conformational analyses have been done using IR spectroscopy and revealed a remarkable influence of surface functionalization on the protein conformation during the adsorption process.

**Keywords:** Electrodeposited; Dicalcium phosphate; Biocompatibility; Morphology; Nanostructuring; Biological fixation

## Introduction

Titanium and its alloys have been a material of choice for many orthopedic implant material and dental implant devices due to their biocompatibility and their good mechanical properties [1]. Despite all these excellent properties, a true adhesion between the bone and the metal surface has not yet been observed because of insufficient bone-implant contact and fibrous encapsulation which may not always ensure proper biomechanical fixation and lead to the failure of medical implants [2]. The need for improved healing response and increased speed of osseointegration of the biomaterial with the host tissue is still a relevant topic. A number of studies have reported the effects of surface chemistry on implant integration with bone and indicated that osteoblasts proliferation and differentiation and protein adsorption by tissue are influenced by implant surface morphology and chemistry [3].

Nanostructuring may produce surfaces with controlled topography and chemistry that could help developing of novel implant surfaces with predictable tissue-integrative properties [4]. It was indicated that the implant surface nanostructuring is a decisive factor in surface cell adhesion and growth, by modulating cell behavior and protein adsorption [5].

Surface chemical composition and local atomic charges are also critical for protein adsorption and cell attachment [6]. Recently, Calcium phosphate compounds CaPs have been widely used as coatings for metallic prostheses to improve their biological properties. Osseointegration of titanium implants coated with biomimetic calcium phosphate has been investigated in pre-clinical comparative models [7]. Studies have demonstrated a higher bone-to-implant contact for biomimetic calcium phosphate coatings than for uncoated ones [8].

Following implantation, the release of calcium phosphate into the peri-implant region increases the saturation of body fluids and precipitates a biological CaP material (such as hydroxyapatite) onto the surface of the implant [9]. The biological fixation of titanium implants to bone tissue is faster with a calcium phosphate coating than without [10]. Other studies [5] indicated that Strontium affects the activity of cells *in vitro*; it decreases the activity of osteoclasts and induces cell apoptosis, resulting in a decrease in bone resorption *in vitro*. Which means that using Sr in a dose dependent manner [11] can enhance endosteal and trabecular bone formation without affecting bone mineralization [10,11]. Thus, it is believed that Sr presence in the interface between the implant and the bone via a calcium phosphate coating will induce the osseointegration, and enhance the success of the implant [12]. Furthermore, doping by Sr ions can influence the nucleation of CaP as Sr ions were reported to reduce the overall rate of CaP crystallization and delay the transformation of amorphous CaP to apatite phases [13].

In the past decade, a lot of studies [14] have been focused on nanostructured TiO<sub>2</sub> thin films grown on Ti and Ti alloys by the

\*Corresponding author: Issa S, University Paris Diderot-Paris 7, U.F.R. Odontologie, 5, rue Garancière 75006, Paris, France, Tel: +33660131120/+33156703036; Fax: +3314675043; E-mail: sabinissa@hotmail.com

Received November 17, 2015; Accepted December 10, 2015; Published December 20, 2015

Citation: Issa S, Azevedo C, Pires R, Cenedese P, Dubot P (2015) Functionalization of Nanostructured TiO<sub>2</sub> Surfaces with Electrodeposited Strontium Doped Calcium Phosphate and Evaluation of BSA Adsorption for Dental Implant Design. J Nanomed Nanotechnol 6: 343. doi:10.4172/2157-7439.1000343

Copyright: © 2015 Issa S, et al. This is an open-access article distributed under the terms of the Creative Commons Attribution License, which permits unrestricted use, distribution, and reproduction in any medium, provided the original author and source are credited.

anodization process in aqueous acetic acid to the 0.5% HF electrolyte [15]. This type of controlled nanostructured surfaces offers the opportunity to create surface reactive sites that cannot exist on traditional TiO<sub>2</sub> due to the extreme low dimensionality of surface nanostructures. Consequently, a better interfacial bonding between a thin film coating and the substrate can be obtained when the oxidized metal surface is nanostructured [16,17]. Cell adhesive proteins can provide attachment sites for osteoblast precursors binding to the implant, which then leads to faster in-growth of bone and stabilization of the implant. Data reported [18] that BSA may have a specific binding interaction with hydroxyapatite which improves the adhesion and proliferation of osteoblasts. These findings suggest that it might be possible to develop better TiO<sub>2</sub> coated with CaP biomaterials through an incorporation of albumin into the mineral matrix to improve cell adhesion and proliferation [19]. Yamaguchi et al. [20] reported that surface modification with BSA led to significant improvement in osteoblast-like cells binding to an electrodeposited CaP coating. Similar observation, but for MC3T3-E1 cells were reported by other authors [19], who have found that BSA adsorption to conventional and nanophase surfaces (including hydroxyapatite) influences the activity of adherent cells. The adsorption of BSA probably affects positively the kinetics of proliferation of the attached cells [21].

According to several studies, the decrease of pH led to an increase in the acidic protein form adsorption and binding affinity [22]. Thus, it's important to study the influence of electrostatic interactions between protein and surface charges on the adsorption process. Functionalized surfaces have been immersed in BSA solution for neutral (7), acidic (4.5) and basic (10.0) pH as both the ionicity of the molecular surface of the BSA and the ionicity of the oxide surface vary in a function of pH value. In this consideration, it's important to mention the point of zero charge (PZC or IEP) that is defined as the pH of the solution (pH<sub>IEP</sub>) for which the overall charge of the surface is zero [23]. When the pH of the solution is lower than the pH<sub>IEP</sub>, a positive global charge is observed on the solid or molecule surface, while for pH values higher than pH<sub>IEP</sub>, a negative global surface charge is observed. In the case of nanoscale objects, the electronic structure gives particular surface ionic sites that can have a very different local charge and reactivity. Bavykin et al. [24], have shown that the PZC of TiO<sub>2</sub> nanotubes is close to 3.0-4.0, indicating a pH value more acid than for traditional forms of anatase type or rutile for macroscopic samples. For the different forms of calcium phosphates, PZC is basic, circa 10.0. For calcium phosphate doped with strontium, the PZC is by 9.0 [25].

Actually, this work is realized in two steps; first, we have studied the nanostructured Ti oxide layer surface with adsorbed calcium phosphate compound. The adsorbed layer topography and chemistry have been studied in the beginning of the deposition process, i.e., for very low CaP coverage ratios (thickness range of some nm as evaluated by SEM images and XPS intensities), in order to highlight the interfacial zone composition. Both X-ray photoelectron spectroscopy (XPS) and infrared spectroscopy (IR) were used to investigate interfacial chemistry and chemical bonds of adsorbed species.

Then in the second part of this work, we studied the adsorption process of BSA on an "acidic" surface (nt-TiO<sub>2</sub>) and two basic surfaces (CaP.nT-TiO<sub>2</sub> and Sr.CaP.nT-TiO<sub>2</sub>).

As secondary and tertiary structures of the protein are strongly pH dependent, pH range chosen in this work concerns the N earth shape form of BSA (globular form) shown in Figure 1, that consists of 55-67%  $\alpha$ -helices, 21%  $\beta$ -sheet, and the rest are turns. At pH less than 4.0, the BSA molecule unfolds into an expanded form (more linear) with 45%  $\alpha$ -helix.

We used IR spectroscopy as a main analytic device to probe protein structure modifications during adsorption process. The use of IR spectroscopy in protein analysis is based on the assessment of the amide bands (Amide I and Amide II) that appear from the amide bonds between amino acids [26]. The most sensitive spectral region to the protein secondary structural components is the amide I band (1700-1600 cm<sup>-1</sup>), which relates to the C = O stretch vibrations of the peptide linkages (approximately 80%) coupled with little in-plane NH bending (<20%). The frequency of this vibration band depends on the nature of hydrogen bonding involving the C = O and NH. The nature of the amino acid side-chain strongly affects the amide I which only depends on the secondary structure of the backbone. Thus, the amide I band is best suited to determine the secondary structure of proteins. The amide II band, (1500-1600 cm<sup>-1</sup>), is attributed to in-plane NH bending (40-60% of the potential energy) and to the CN stretching vibration (18-40%). Amide II is affected by side-chain vibrations but the correlation between secondary structure and frequency is not that accurate when compared to the amide I region [27]. The absorption in the range 1650-1660 cm<sup>-1</sup> is assigned to  $\alpha$ -helix structure in aqueous environments. The vibration of  $\beta$ -sheet can be seen in the region (1620-1640 cm<sup>-1</sup>) and this position can be affected by varying strengths of the hydrogen bonding and transition dipole coupling in different  $\beta$ -strands.  $\beta$ -turn vibration is around (1662-1690 cm<sup>-1</sup>). The secondary structure of protein can be also determined from the amide II band, but the correspondance between IR spectra and secondary structure is more complex than in the amide I region because bands in the amide II region have not been well studied. In amide II region, bands between 1540-1550 cm<sup>-1</sup> are regraded as  $\alpha$ -helix and the  $\beta$ -sheet vibration is the range 1520-1530 cm<sup>-1</sup>.

Actually, the choice of BSA was made due a practical and technical point of view in our functionalization, cos protein adsorption was evaluated by infrared spectroscopy to target any change of protein confirmation so in addition to its biological role, it was chosen as it's a soft small protein that can be captured by IR spectroscopy.

However, it's important to evaluate the adsorption of other proteins such as fibronectin on our functionalized surfaces but spectroscopic information on bigger protein is less obvious (BSA is only about 60

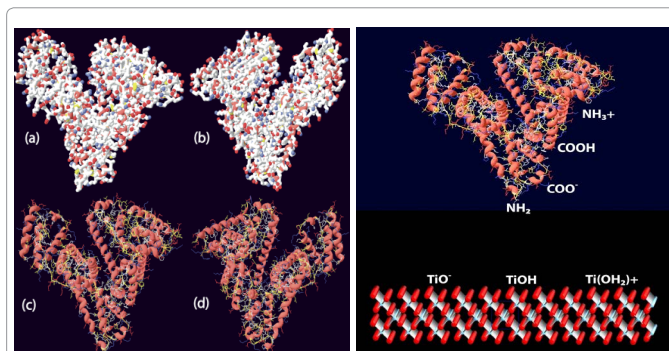


**Figure 1:** N form of the globular structure of BSA.

Figures (a) and (b) shows a diagram of "ball & sticks" type with negatively ionized groups (COOH) in red and positively ionized groups (R-NH<sub>2</sub>, for example) in blue. (a) and (b) show a front and back view of the form N. (c) and (d) show a representation of the secondary structures with  $\alpha$ -helices and side chains (acidic =red, basic=blue). We notice the relatively homogeneous distribution of potentially positive and negative charges on the molecular surface. Right side of the picture: BSA and surface groups implicated in acid-base interactions. Representations are obtained with Swiss PDB viewer 4.01.

kDa, whereas fibronectin is much larger (almost 10 times) with about 460 kDa). Thus, BSA has been chosen as a test protein to evaluate clearly the influence of surface functionalization on biomolecules adsorption processes. Anyway, this study could be a database to test conformational changes of small size's protein on our surfaces which will be followed by further studies using other proteins that enhance the cellular adhesion process.

In this work, we used infrared spectroscopy in the reflection-absorption mode for different immersion periods in protein solutions and IR spectrum evolution has been followed. Amide I and Amide II bands shape have been deconvoluted into characteristic components of protein secondary structures and conformational states have been deduced.

## Materials and Methods

Acetic acid (normapur, 96%) and fluorhydric acid (38-40%) were respectively purchased from WWR and Merck. Strontium chloride hexahydrate was purchase from Fluka. Calcium chloride dehydrate, trisodium phosphate dodecahydrate and BSA (>98%) were a Sigma-Aldrich products and titanium foil (99.99%, 1.0 mm thick) was purchased from Goodfellow.

Fabrication of TiO<sub>2</sub> nanotube arrays via anodic oxidation of titanium foil in a fluoride-based solution was first reported by Grimes and co-workers [8]. Further studies focused on precise control and extension of the nanotube morphology [28], length and pore size [29], and wall thickness [30]. The Ti foils were polished down to 4000 grade SiC paper and then cleaned by sonication (180 s) in acetone-alcohol mixture (50%). Titanium foils were anodized (EGG Princeton Applied Research potentiostat A263 using a three-electrodes electrochemical cell with a platinum foil as cathode. The titanium samples were anodized for 600 s. The addition of acetic acid to the 0.5% HF electrolyte in a 1:7 ratio results in more mechanically robust nanotubes without changing in their shape and size [31].

Concerning the CaP coating, previous studies have been mostly realized by soaking the samples in SBF solutions [32]. This process generally takes long immersion periods (few days) [33] to precipitate CaP on the TiO<sub>2</sub> nanotubes. In this work, we realized the CaP deposition from acidic aqueous solutions by pulsed electro-deposition at room temperature. A similar deposition process have been recently applied by Kar et al. [16] and showed an enhancement of the coating adhesion. In our work, potential pulses (PP) were repeatedly set at -2.0 V for 0.5 s immediately followed by 0.0 V relaxation potential for 0.5 s. During negative potential pulse, H<sub>2</sub>O reduction leads to the creation of hydroxyl in the surface vicinity, which increases the local pH and CaP precipitation.

Calcium phosphate solution (CaP<sub>sol</sub>) was obtained by mixing 2.20 g of (CaCl<sub>2</sub>·2H<sub>2</sub>O) with 2.20 g of (Na<sub>3</sub>PO<sub>4</sub>·12H<sub>2</sub>O) in 1000 ml of deionized water. The pH solution was adjusted to 4.0 with HCl. For mixed strontium-calcium phosphate solutions (CaP<sub>Sr</sub>sol), we have used three percentages of Sr (10%, 20%, 30%) by adding respectively 0.27 g, 0.54 g or 0.81 g of (SrCl<sub>2</sub>·6H<sub>2</sub>O) in the previous CaP solution. This leads to CaP solutions with [Ca<sup>2+</sup>] = 0.01 M, [PO<sub>4</sub><sup>2-</sup>] = 0.006 M and [Sr<sup>2+</sup>] = 0.001, 0.002 or 0.003 M.

XPS measurements were performed using a MAC II RIBER photoelectron spectrometer with non-monochromatized Al Kα excitation (hν = 1486.6 eV). The compositions of the surface film were determined by measuring integrated photo-peaks intensities after a Shirley background subtraction. The peaks areas were corrected from

sensitivity factors [34]. The X-ray spot diameter was 5 mm<sup>2</sup>. Survey spectra were acquired with an energy step of 1.0 eV, while it was 0.05 eV for core level windows. Acquisition time was 100 ms per step in all the case. The analysis chamber base pressure was by 2.0 10<sup>-10</sup> torr. IR spectra were obtained by a NICOLET 6700 IR spectrometer equipped with a VEEMAX accessory allowing reflection-absorption experiment with an infrared beam incidence angle of 70°. Incidence angles between 45° and 80° were tested and the 70° value was chosen for reflection-absorption experiments as it gives a good signal to noise ratio. Spectra have been averaged over 128 scans and the resolution was set to 4.0 cm<sup>-1</sup>.

Images were realized with a field emission scanning electron microscope (FE-SEM, LEO) operating at 5.0 kV. The surface composition of the samples was also controlled using energy dispersive spectroscopy (EDS).

## Results and Discussion

### SEM analysis

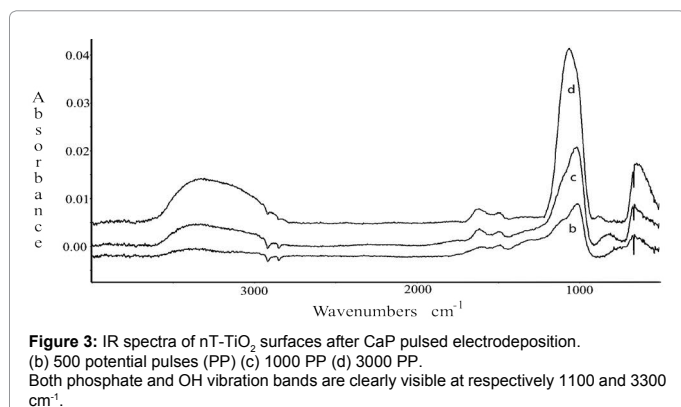
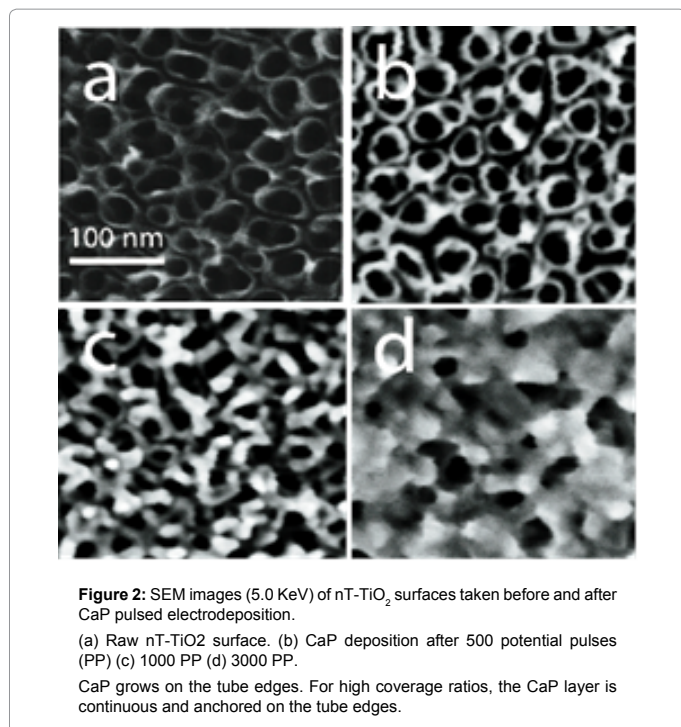
Anodized titanium surface in HF solution presents amorphous TiO<sub>2</sub> nanotubes aligned perpendicularly to the sample surface. Tubes diameter is about 35 nm at an operating potential of 8.5 V. Samples were rinsed and conserved in deionized water (22 MOhms) before CaP pulsed electrodeposition. Figure 2 shows SEM images of the Ti nanostructured surface (nT-TiO<sub>2</sub>) at different deposition time: (a) raw nT-TiO<sub>2</sub>, (b) electrodeposited CaP after 500 potential pulses (PP), (b) after 1000 PP and (b) after 3000 PP. As it can be seen on (a), (b) and (c), the deposit is growing on the edges of the TiO<sub>2</sub> nanotubes, indicating that tubes edges are the most reactive sites of the nT-TiO<sub>2</sub> surface.

From a crystal growth point of view, tube edges must be very reactive areas compared to tube walls and can be considered as preferred areas for adsorption process like steps on a plane surface. For high coverage ratios, CaP nano-particles anchored to tube edges get bigger and gathered to finally cover the whole surface.

### Infrared spectroscopy and XPS analysis of functionalized surfaces

CaP deposit growth has also been investigated by infrared spectroscopy, allowing a chemical characterization of the CaP clusters according to their size. The IR spectra shown in Figure 3 are dominated by a broad absorption band located near 1000 cm<sup>-1</sup> that is characteristic of phosphate vibration modes [35].

For phosphate species H<sub>(n)</sub>PO<sub>(4)</sub><sup>(3-n)</sup> (n = 0-3), the region between 800 and 1300 cm<sup>-1</sup> contains the majority of the stretching vibration modes for P-O bonds. We can observe that the band shape evolves with the coverage ratio, i.e., with the CaP nano-particles size. Vibration modes of phosphate compounds strongly depend on the PO<sub>4</sub> entities coordination. For example, the tetragonal PO<sub>4</sub><sup>3-</sup> ion exhibits four different vibrations, the symmetric stretching (ν<sub>1</sub>), the symmetric bending (ν<sub>2</sub>), the asymmetric stretching (ν<sub>3</sub>) and the asymmetric bending (ν<sub>4</sub>). The ν<sub>1</sub> (symmetric stretching) and the ν<sub>3</sub> (asymmetric stretching) vibration can be used to identify the molecular symmetry of the PO<sub>4</sub><sup>3-</sup> entity and the coordination environments. As phosphoric acid is a triacid, the protonation level significantly affects the PO<sub>4</sub><sup>3-</sup> molecular symmetry. When fully deprotonated, PO<sub>4</sub><sup>3-</sup> has tetrahedral (Td) symmetry and the IR spectrum shows a single ν<sub>3</sub> asymmetrical vibration near 1006 cm<sup>-1</sup> and the ν<sub>1</sub> vibration is not active [36]. In the case of monodentate mononuclear complex the ν<sub>3</sub> asymmetrical vibration is located by 1030 cm<sup>-1</sup> while it is shifted to higher wavenumbers near



1050 cm<sup>-1</sup> for bidentate binuclear complexes [37]. Mono-protonated (HPO<sub>4</sub><sup>2-</sup>) species have a local C<sub>3v</sub> symmetry and the ν<sub>3</sub> vibration splits into two components located at 1080 and 990 cm<sup>-1</sup>. There is also ν<sub>1</sub> band near 850 cm<sup>-1</sup> that becomes active.

Further protonation leads to H<sub>2</sub>PO<sub>4</sub><sup>-</sup>, which leads to a symmetry lowering from C<sub>3v</sub> to the C<sub>2v</sub>. The ν<sub>3</sub> vibration splits into two bands, therefore, there are a total of three bands at 1160 cm<sup>-1</sup>, 1074 cm<sup>-1</sup> and 940 cm<sup>-1</sup>. Moreover, even if the local symmetry is strongly dependent on the phosphate entity protonation, symmetry can also be affected by ligand coordination in the case of a bulk compound or in an adsorption state on a solid surface.

According to the wave-numbers values for CaP coating on nT-TiO<sub>2</sub> surface, we mainly observe a broad peak in the phosphate vibration region. This peak is composed of two apparent components located near 1030 and 1100 cm<sup>-1</sup>, with a weak shoulder in the 800-900 cm<sup>-1</sup> range. These bands location are consistent with ν<sub>3</sub> and ν<sub>1</sub> modes of phosphate entity. As these two bands are located at higher wavenumber than for free HPO<sub>4</sub><sup>3-</sup> entity, we suppose a bidentate coordination as for PO<sub>4</sub><sup>3-</sup> [36,37]. As the CaP clusters size increase, the 1100 cm<sup>-1</sup> completely

dominates the IR spectra. This band can be attributed to HPO<sub>4</sub><sup>2-</sup> in poorly crystallized CaP compound. The IR spectra of Figure 3 also reveal a broad absorption band located by 3300 cm<sup>-1</sup> that is correlated with hydrogen bonds induced by hydroxyl groups and water present in the compound. We can also observe low intensity peaks by 1500 cm<sup>-1</sup> which could be attributed to carbonates.

The obtained spectra, and the symmetric and asymmetric vibrations at 1030-1100 and 900 cm<sup>-1</sup> confirmed the amorphous apatitic nature of the CaP films formed on the substrates for different coverage ratios.

Concerning XPS experiments, all spectra show a positive energy shift of 1.7 eV referenced to the C1s peak at 285.0 eV and the energy scale has not been corrected. Figure 4 presents the XPS spectra of 500 PP (a) and 3000 PP (b) CaP deposited onto nT-TiO<sub>2</sub>. We observe that the substrate Ti signal (2p<sub>3/2</sub> core level) is very low on Figure 4b, meaning that the adsorbed compound screens it. Ca<sub>2p</sub>, P<sub>2p</sub> and O<sub>1s</sub> core level signals respectively at 348.2 eV, 134.2 eV and 532.2 eV confirm SEM and IR spectroscopy observations, i.e., a calcium phosphate compound has grown on top of the nT-TiO<sub>2</sub> surface.

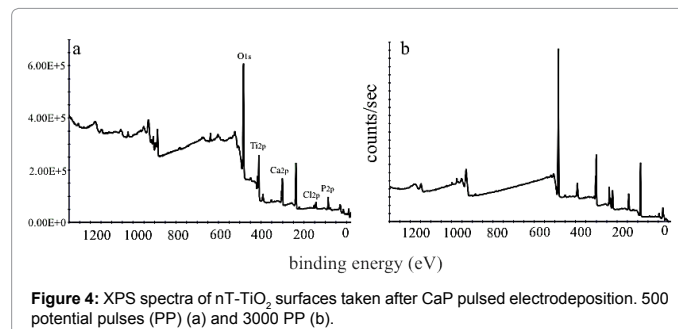
XPS survey spectra also reveal the presence of carbon contamination at 286.7 eV and a small component at 290.6 eV due to carbonates. As Ar sputtering strongly reduces the C<sub>1s</sub> peak, we conclude that the carbon contamination is mainly localized at the ultimate surface of the coating.

The chloride ions Cl<sub>2p</sub> (199.5 eV) peak was assigned to the adsorption of Cl<sup>-</sup> ions at the outermost surface [38]. These adsorbed Cl<sup>-</sup> may facilitate the electrostatic adsorption of Ca<sup>2+</sup> and thus trigger the heterogeneous precipitation of a CaP phase by enhancing the negative surface charge [39].

To get further inside the coatings chemistry, higher resolution core level spectra have been recorded, and especially for the P<sub>2p</sub> + Sr<sub>3d</sub>, Sr<sub>3p</sub>, O<sub>1s</sub>, and Ca<sub>2p</sub> core levels. In Figure 5, the O<sub>1s</sub> peak clearly shows a broad structure that can be deconvoluted into basic Gaussian components characterized by FWHM (Full Width at Half Maximum) of 2.1 eV.

In the case of pure CaP coating, 5 peaks are necessary to realize the O<sub>1s</sub> deconvolution, while for mixed Sr-CaP coatings, the O<sub>1s</sub> structure is thinner, and only 3 peaks are needed. In each case, the higher binding energy component, located at around 534.2 eV, is attributed to H<sub>2</sub>O specie [40]. This is coherent with a highly hydrated compound. The two peaks near 532.2 eV and 533.0 eV can be assigned to O<sub>1s</sub> of P-O and O<sub>1s</sub> of P-OH respectively.

For these two components an area ratio of 3 is obtained by the deconvolution process, and we can thus conclude a mono-protonated (HO-PO<sub>3</sub>)<sup>2-</sup> entity. In the case of the pure CaP coating, the peaks at 530.8 eV and 529.0 eV can be assigned to hydroxyls [36,41] or O-Ca bonds that are not present when Sr ions are incorporated into the film. When Sr is incorporated in the CaP solution, Sr<sub>3d</sub> and Sr<sub>3p</sub>



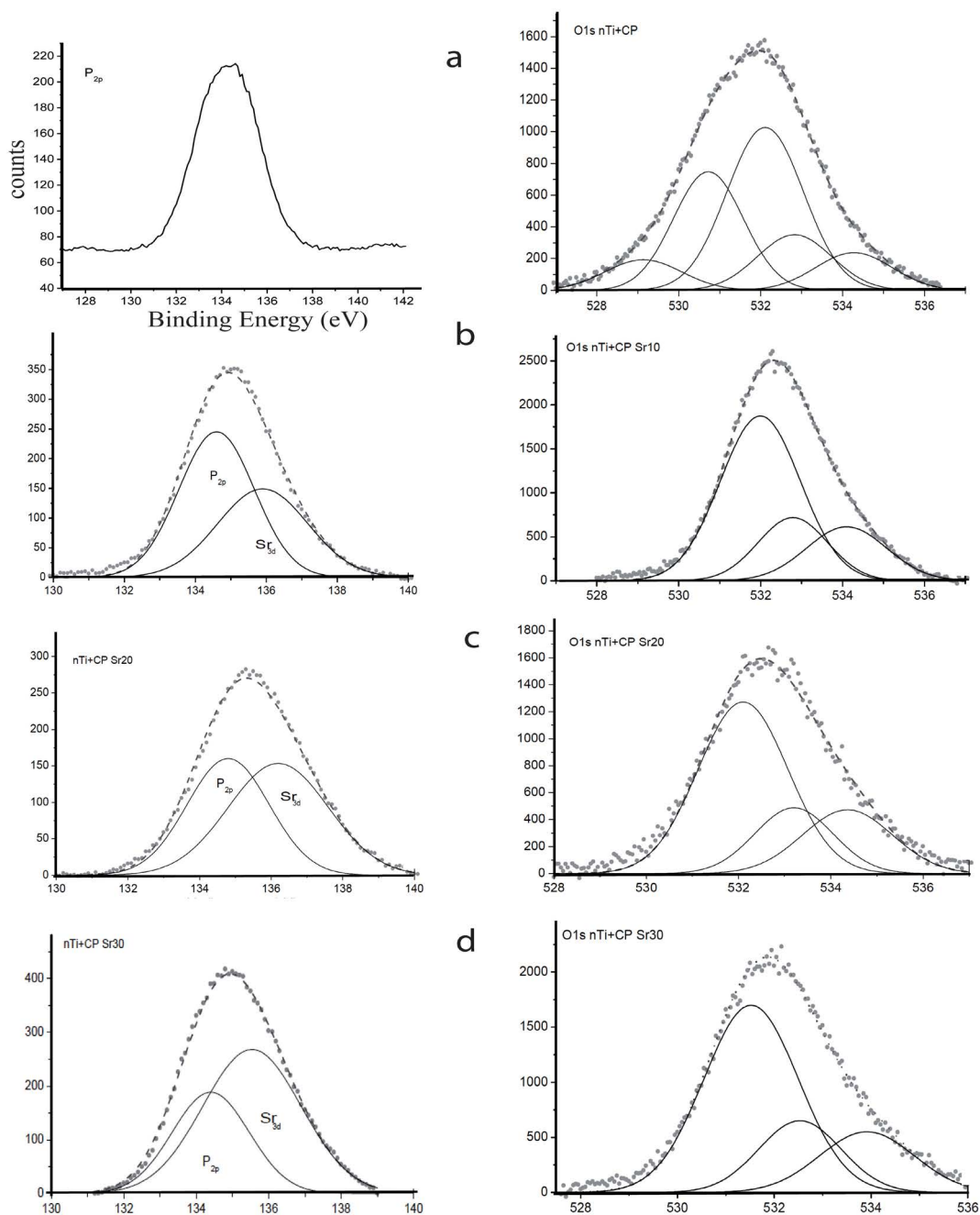


**Figure 5:** P<sub>2p</sub> and O<sub>1s</sub> XPS spectra of nTi-TiO<sub>2</sub> surfaces coated with Sr doped CaP for 3000 PP with respectively: 0% Sr (a), 10% Sr (b), 20% Sr (c) and 30% Sr (d) (% Sr atomic percentage referred to Ca).

photoelectron peaks are clearly present in the spectra. The Sr<sub>3d</sub> overlaps with P<sub>2p</sub> core level giving a broader structure by 134.2 eV. Nevertheless, this two peaks structure can be easily deconvoluted with a peak located at 134.2 eV (P<sub>2p</sub>) and a broader peak (FWHM = 3.2 eV) located at 136.4 eV (Sr<sub>3d</sub>).

Concerning the Ca<sub>2p</sub> core level, the two peaks structure (2p<sub>3/2</sub> at 348.2 eV and 2p<sub>1/2</sub> at 351.8 eV) is shown in Figure 6. As for the O<sub>1s</sub> level, the Ca<sub>2p</sub> doublet clearly present a broadening with new components that reveals additional chemical bonds in the case of pure CaP coating (Figure 6a) that are not present when Sr is added into the film.

When measured peaks areas are corrected by sensitivity factor one can tentatively interpret semi-quantitatively our results and we obtained the following surface concentrations ratios that are presented in Table 1. From Table 1, we can conclude that the Sr/Ca ratio in the deposited film agrees with the solution concentrations, what was not obvious as many chemical or physical factors can enhance one of the element deposition in the electrodeposition process.

Getting further inside XPS quantification and compound chemistry identification, we can deduce from Table 1 that for pure CaP, calcium to phosphorus ratio is around [Ca]/[P] = 1.30. Many different

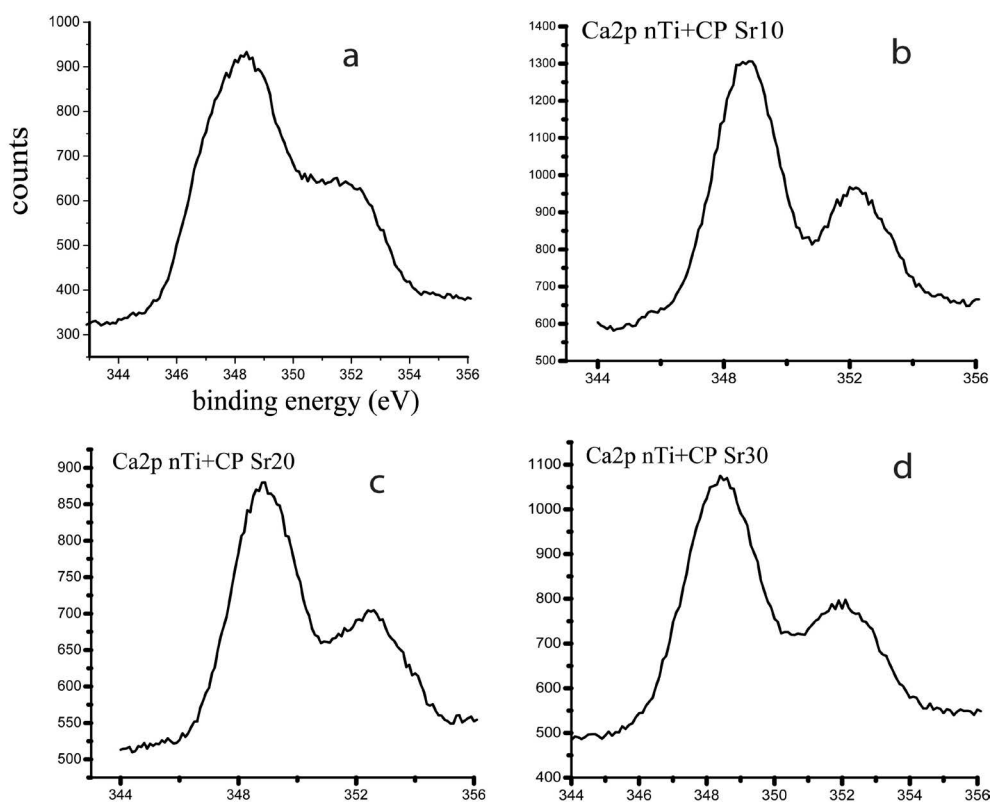


**Figure 6:** Ca<sub>2p</sub> XPS spectra of nTi-TiO<sub>2</sub> surfaces coated with Sr doped CaP for 3000 PP with respectively: 0% Sr (a), 10% Sr (b), 20% Sr (c) and 30% Sr (d) (% Sr atomic percentage referred to Ca). One can notice the larger width of the Ca<sub>2p</sub> levels for pure CaP coating.

	[O]/[P]	[P]/[Ca]+[Sr]	[Sr]/[Ca]	[Sr]/[Ca]+[Sr]	[O <sub>H2O</sub> ]/[O <sub>tot</sub> ]	[O-P]/[HO-P]
CP pure	5.20	1.31	0.00	0.00	0.16	2.95
CP Sr10	5.90	1.03	0.15	0.13	0.21	3.10
CP Sr20	6.02	0.95	0.29	0.22	0.22	2.85
CP Sr30	5.96	0.97	0.46	0.32	0.23	2.90

**Table 1:** Element concentration ratios deduced from peaks area corrected with sensitivity factors.

calcium phosphates (CPs) can exist and are mainly distinguishable by their [Ca]/[P] ratio. In alkaline conditions, hydrated amorphous tricalcium phosphate ( $\alpha$ -TCP, [Ca]/[P]  $\approx$  1.5) is most widely found by precipitation in aqueous solution [42].

When the pH is more acidic, ACPs may contain HPO<sub>4</sub><sup>2-</sup> ions giving a compound characterized by a lower [Ca]/[P] value but always greater than 1.0. Crystalline CaP phases like OCP and calcium-deficient apatite have been observed [43]. Moreover, ACP composition can change with ageing as proposed by Heughebaert et al. [44] and internal hydrolysis between PO<sub>4</sub><sup>3-</sup> and H<sub>2</sub>O can occur in ACP gels, leading to HPO<sub>4</sub><sup>2-</sup> and OH ions formation.

This type of reaction can exist during our pulsed electrodeposition process. It's also suggested that during the cathodic pulse (-2.0 V), water reduction produce a high hydroxyl concentration near the n-TiO<sub>2</sub> electrode surface in an acidified solution that contains H<sub>2</sub>PO<sub>4</sub><sup>-</sup> and HPO<sub>4</sub><sup>2-</sup> entities, leading to a complex precipitation with HPO<sub>4</sub><sup>2-</sup> and OH ions.

In the case of an amorphous disordered compound ( $\alpha$ -ACP) elaborated in alkaline medium, with calcium deficiency, a range of

composition of  $\alpha$ -ACP can be represented by the following formulae: Ca<sub>9-y</sub>(PO<sub>4</sub>)<sub>6-x</sub>(HPO<sub>4</sub>)<sub>x</sub>(OH)<sub>x-2</sub>.

From the calcium to phosphorus ratio [Ca]/[P] = 1.30 found by XPS, we can expect a compound like Ca<sub>4</sub>(HPO<sub>4</sub>)<sub>3</sub>(OH)<sub>2</sub>, Ca<sub>4</sub>PO<sub>4</sub>(HPO<sub>4</sub>)<sub>2</sub>(OH) or Ca<sub>4</sub>(PO<sub>4</sub>)<sub>2</sub>(HPO<sub>4</sub>)<sub>2</sub>(OH) [45]. The O<sub>1s</sub> and P<sub>2p</sub> peaks make the rich OH compound Ca<sub>4</sub>(HPO<sub>4</sub>)<sub>3</sub>(OH)<sub>2</sub> the most probable (x = 6 and y = 1 in the preceding formulae).

This result matches also perfectly the broadening of the Ca<sub>2p</sub> peak as the hydroxyls present in the structure must shift the Ca<sup>2+</sup> cation core levels to higher binding energy compared to bonding with phosphate entities (Figure 6).

The situation of the Sr doped CaP deposition is rather different and the [Ca]/[P] ratio is near 1.0, so we can expect a compound like Ca<sub>1-x</sub>Sr<sub>x</sub>HPO<sub>4</sub> in accordance with the O<sub>1s</sub> and P<sub>2p</sub> deconvolution. The difference of compound chemistry and structure between pure and Sr doped CaP coating is not surprising as foreign ions like Sr<sup>2+</sup> ions can strongly affect CaP compounds structure and stability. In fact X<sup>2+</sup> cations like Sr<sup>2+</sup>, Zn<sup>2+</sup> or Mg<sup>2+</sup> are known to favor the less compact

calcium phosphate structure (TCP, lamellar DCPD or DCPA) compared to the more complex HAP phase [46]. For example, the Sr<sup>2+</sup> ionic radii is about 12% higher than the Ca<sup>2+</sup> one, which gives greater steric constraint adaptability in less compact structures. It can be noticed too that [O]/[P] ratio is greater than 4.0 meaning that the coatings are hydrated. From the O<sub>1s</sub> deconvolution, we observe [O<sub>H<sub>2</sub>O</sub>]/[O] ≈ 0.20 which means that 20% of the oxygen signal is coming from H<sub>2</sub>O for almost all compounds studied in this work.

This difference of chemical structure induced by Sr is also attested by a chemical shift on the O<sub>1s</sub> and P<sub>2p</sub> core levels when strontium is incorporated in the deposit. For low [Ca]/[P] calcium to phosphorus ratio like in DCPD (Dicalcium phosphate dihydrate; CaHPO<sub>4</sub>·2H<sub>2</sub>O), Chusuei observed an increase of 0.5 eV for O<sub>1s</sub> and P<sub>2p</sub> binding energy between ACP and DCPD, while the Ca<sub>2p</sub> peak is located at the same binding energy [47]. When we refer binding energies to the Ca<sub>2p</sub> level (avoiding change in work function between samples), we find that O<sub>1s</sub> and P<sub>2p</sub> binding energy are respectively shifted of +0.4 eV and +0.5 eV for the strontium doped deposit.

Figure 7 reveals that IR spectra are markedly different for Sr doped CaP coating. For all spectra (Figure 7a-7d), at least four bands are clearly visible in the phosphate vibration modes region: 885, 1120, 1180, 1243 cm<sup>-1</sup>. According to Casciani et al. [48] these bands can be attributed to CaHPO<sub>4</sub> compound. The band located at 1243 cm<sup>-1</sup> is associated with the local OH in plane bending mode of HPO<sub>4</sub> group [49]. Bands at 885, 1120 and 1180 cm<sup>-1</sup> are characteristic of delocalized modes in CaHPO<sub>4</sub> [50]. Compared to Casciani infrared spectra, the absorption bands of Figure 7 are much larger, probably due to a less disordered compound in the case of the electrodeposited coating. From a biological point of view, many studies reported that non-apatitic strontium doped CaP coating is preferable to that apatitic one as it is known that the soluble TCP like phases is responsible for a beneficial release of Sr<sup>2+</sup> in solution during interactions between the implant coating and biological fluids [3].

Based on our XPS and IR results, we can expect calcium phosphate compound similar to Dicalcium Phosphate Anhydrous (DCPA; CaHPO<sub>4</sub>) or Dicalcium phosphate dihydrate (DCPD; CaHPO<sub>4</sub>·2H<sub>2</sub>O) that are more resorbable than ACP and HAP [51] when Sr<sup>2+</sup> is incorporated in the deposit. Concerning CaSrP coatings structure, it appears to be more ordered than CaP coatings as revealed by the ν<sub>4</sub> vibration mode of phosphate entities (located by 604 cm<sup>-1</sup>). Following Farlay et al. [52] a mineral crystallinity index can be defined as being inversely proportional to the FWHM of the ν<sub>4</sub> vibration mode, the narrower the peak is, the higher the crystallinity index. In order to validate the using of the width at half-height ν<sub>4</sub> vibration mode as a crystallinity index by infrared spectroscopy, this latter has been compared on same samples with the crystallinity index measured by the Shemesh method [53]. Figure 8 shows this spectral region and confirms narrower peaks in the case of Sr doped Cap coating (Figure 8b) compared to the non-doped CaP coating (Figure 8a).

### BSA adsorption on functionalized TiO<sub>2</sub> surfaces

**Protein adsorption analysis by Infrared Spectroscopy:** In this part of work, we have investigated the influence of nanostructured TiO<sub>2</sub> surface previously studied on the adsorption of BSA. BSA is found in high concentrations (50.0 g.L<sup>-1</sup>) in the blood medium but a lower BSA concentration of 0.1 g.L<sup>-1</sup> was used in this work to reduce kinetic adsorption and to study more easily the low coverage regime.

At each time step (surface immersion for a given period), the sample is finally rinsed in deionized water, dried under pure N<sub>2</sub> flow and analyzed by IR. The IR spectrum allows us to evaluate the amount of protein adsorbed

and the shape of the amide absorption bands gives us a clue of the evolution of the secondary and tertiary structure of the protein.

In order to qualitatively characterize the adsorption of BSA according to physical parameters such as the nature of the surface or the pH of the solution, we measured infrared spectra depending on the amount of BSA adsorbed and decomposed the amide I and II absorption bands (Figure 9). The evolution of the intensities A<sub>I</sub> = f(t) and A<sub>II</sub> = g(t), can reveal the maximal intensities I<sub>max</sub> at coverage saturation and the slope of the tangent at the origin that is related to the adsorption speed for low coverage. Moreover, the total intensity of the amide I band (A<sub>I</sub>) can be compared to the total intensity of amide I and amide II (A<sub>I</sub> + A<sub>II</sub>), the ratio A<sub>I</sub>/(A<sub>I</sub> + A<sub>II</sub>) being related to structure modification and / or adsorption geometries [54]. From the measurements amide I and

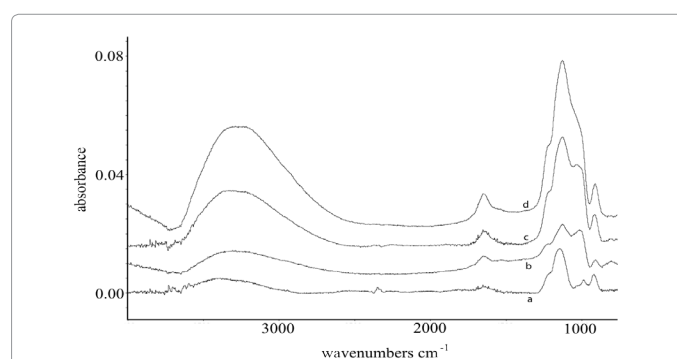


**Figure 7:** IR spectra of 30% Sr doped CaP Coating for 500PP, 1500PP, 3000PP and 5000PP (a, b, c and d respectively). While the broad band characteristic of bounded OH is still evident (OH stretching), the phosphate band presents a different structure when Sr<sup>2+</sup> is substituted to Ca<sup>2+</sup>.

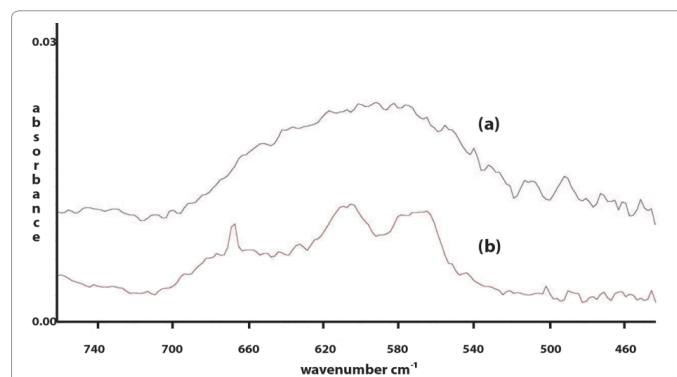


**Figure 8:** IR spectra of 30% Sr doped (b) and non doped (a) CaP coating for 5000PP. The broader the PO<sub>4</sub> ν<sub>4</sub> vibration mode, the less crystalline is the deposit.

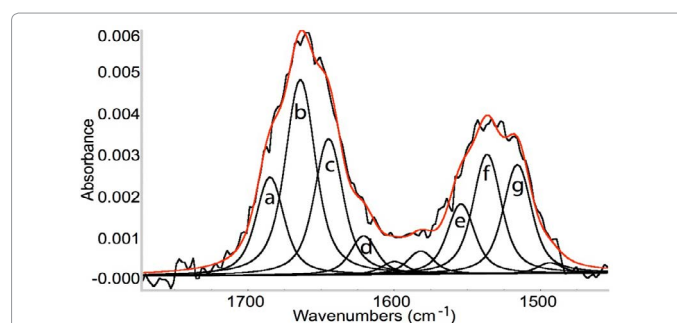


**Figure 9:** Amide I and II decomposition following peptide secondary structures. (a) turns and random coils, (b) helix α, (c-d) u sheet, (e) turns, (f) helix α, (g) α sheet. Peaks near 1580 cm<sup>-1</sup> can be attributed to amino acids side chains.

amide II band intensities we can define a parameter  $R = I_{AI} / I_{AII}$ . It has been shown by Rothschild et al. that R value is related to the average orientation of helix  $\alpha$  relatively to the surface on which it is adsorbed [54]. In the case of a single helix  $\alpha$  lying on the surface, a strong intensity of the amide I band is expected while for amide II it is a low intensity. In the case of a perpendicular direction to the surface plane, the intensity of the amide II band is expected to increase strongly as compared to the intensity of the band amide I [55].

In the case of a complex protein structure, this parameter R gives us only average information on the molecular orientation of the whole protein as this protein consists of several helix  $\alpha$  segments. Note that helix  $\alpha$  segments distribution is rather isotropic for the N form of BSA as it can be seen in Figure 1, while in the case of BSA denaturation, on the contrary most of the helices are oriented in the direction of the axis of elongation of the protein and parallel to the surface for a flat adsorption geometry.

In the case of films with highly organized molecular layer consisting of simple molecules containing single helix  $\alpha$  segment, the ratio R can be expressed in terms of the angle between the axis of the helix and the surface plan. Ignacio et al. give the following relationship (equation (1)) [55]:

$$R[\theta] = K \frac{\frac{1}{2}(3 \cos^2 \theta - 1) \frac{1}{3} (3 \cos^2 \theta_i - 1) + 1}{\frac{1}{2}(3 \cos^2 \theta - 1) \frac{1}{3} (3 \cos^2 \theta_i - 1) + 1} \quad (1)$$

Wherein  $\theta$  represents the angle of the helix axis to the surface,  $\theta_i$  is the angle of the dipole moment of the vibrational transition of the amide I band and  $\theta_{ii}$  angle of the dipole moment of the transition of the amide II band [56].

For a more complex molecule like BSA, an average value of the parameter R can be estimated from the angle of helix  $\alpha$  segments distribution inside the shape form protein for a given adsorption geometry of the whole BSA. This average R value can be calculated by weighted  $R(\theta)$  given above, using the formula (2) :

$$\bar{R} = \sum_{\theta_i} R(\theta_i) P(\theta_i) = \sum_{\theta_i} R(\theta_i) \frac{N(\theta_i)}{N_{tot}} \quad (2)$$

$N(\theta_i)$  is the number of helix  $\alpha$  with  $\theta_i$  angle to the surface;  $N_{tot}$  is the total number of helix  $\alpha$  inside BSA. In the case of a configuration of "End on" adsorption, we estimate  $R_{EO} = 2.3 \pm 0.1$ , whereas in the case of adsorption "Flat", we obtain  $R_F = 3.0 \pm 0.1$ . The variation of R parameter is weak but significant for these two extreme cases of adsorption geometry for the N form of BSA.

In the case of adsorption with "denaturation" and transformation from the N form to a more extended unfolded form (form E or form F), interactions with the substrate will give a majority of helices  $\alpha$  with their axis closely parallel to the surface, and a value of R is significantly lower and close to 0.80

**Results:** The amount and the structural change of adsorbed protein is analyzed through amide I intensity and components as well as the R parameter previously defined.

The kinetic monitoring of infrared spectra in the region of the principal modes of vibration of the BSA is shown in Figure 10 for the functionalized surface of TiO<sub>2</sub> (Sr.CaP.nT-TiO<sub>2</sub> (30% Sr)) for pH = 4.5 (a) and pH = 7 (b). The trends are the same for different deposits of Sr.CaP so for sake of clarity we only show those with 30% Sr.

For each kinetic, we present the infrared spectra for immersion time of 5 s, 10 s, 20 s, 30 s, 60 s and 120 s, after 120 s the IR signal shows no evolution.

In each case studied in this work, we observe a signal evolution that depends on both the nature of the surface and the pH value as revealed by the intensity level and the distribution of bands which compose the amide I peak.

A more detailed analysis, including the composition of the amide I peak, is therefore desirable and was realized from the 4 components mentioned above. To achieve this spectral decomposition, we used the OMNIC software by setting the values of the vibrational frequencies and the width at half height of each band with defined constraints ( $\pm 4.0 \text{ cm}^{-1}$  and for the frequencies  $12.0 \pm 3.0 \text{ cm}^{-1}$  for widths). The bands shape is assumed to be of gaussian type.

Several negative absorption peaks around  $1100 \text{ cm}^{-1}$  were observed which can be associated with a loss of phosphate entities concomitant with the adsorption of BSA (Figure 10b). We note that this phenomenon is pH and surface dependent since it occurs only for BSA adsorption at pH 7.0 on the surface of CaP.nT-TiO<sub>2</sub> and Sr.CaP.nT-TiO<sub>2</sub> (Sr 30%). This concomitant disappearance of phosphate ions and adsorption of BSA indicates a process of molecule-surface interaction with ions exchange, deprotonated carboxyl groups pH 7 of BSA can substitute  $\text{PO}_4^{3-}$  or  $\text{HPO}_4^{2-}$  ions, which are weakly bound to the surface of the CaP deposit.

Figure 11 shows the evolution of the total intensity of the amide I and II bands according to deposition time in the different conditions studied in this work. All curves have a similar appearance with a monotonous variation of the intensity following an exponential law  $I = I_{max}(1 - \exp^{-t})$ . This type of evolution is characteristic for the formation of a single molecular layer (no simultaneous multi-layer growth or layer by layer growth) and indicates that once adsorbed on the surface, the protein layer presents to the aqueous solution an

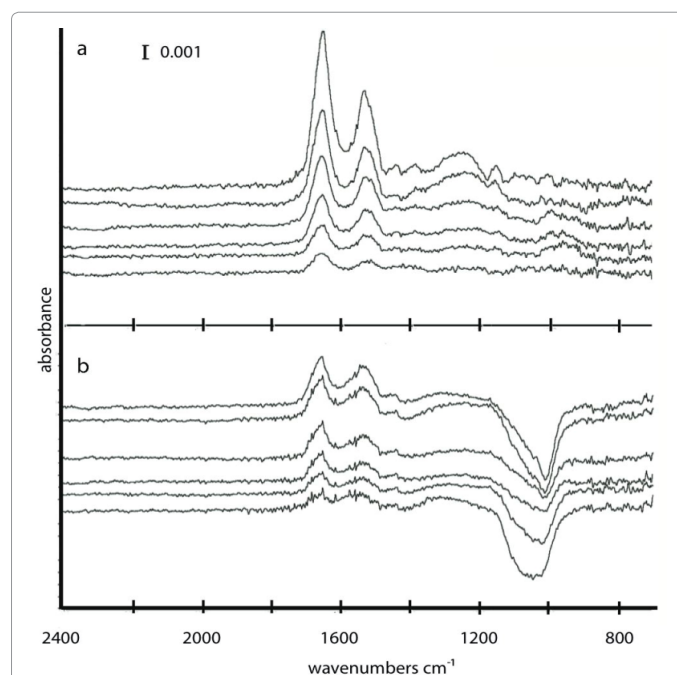
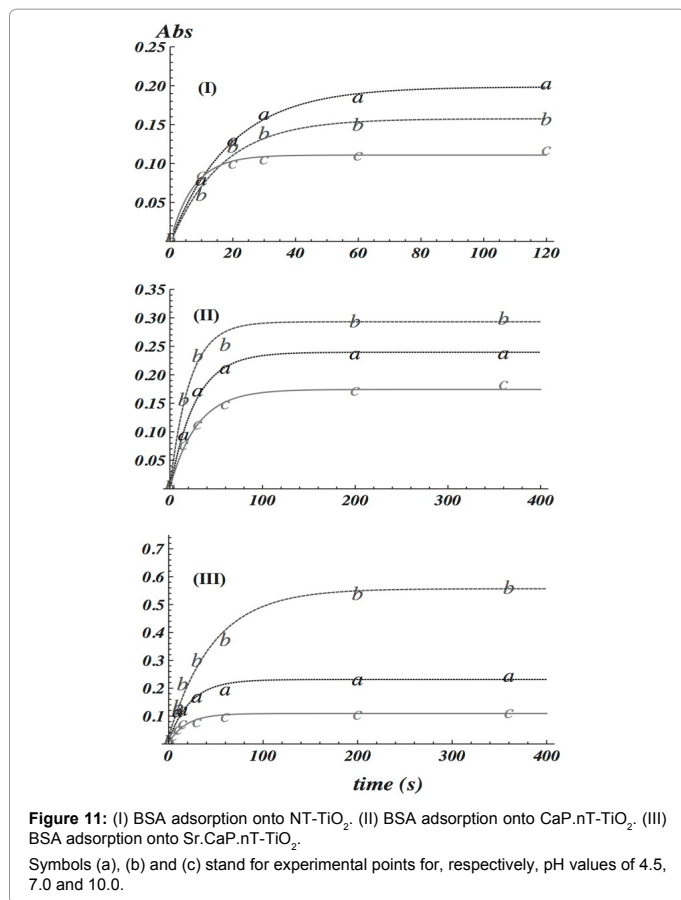


**Figure 10:** Kinetic monitoring of infrared spectra in the region of the principal modes of vibration of the BSA (by  $1500\text{-}1600 \text{ cm}^{-1}$ ) for the functionalized surface of TiO<sub>2</sub> (Sr.CaP.nT-TiO<sub>2</sub> (30% Sr)) for pH = 4.5 (a) and pH = 7 (b). Remark phosphate P-O vibration disappearance when BSA adsorbs for neutral pH. Each kinetic presents the IR spectra for immersion time of 5s, 10s, 20s, 30s, 60s and 120s (bottom to top).



inactive surface for molecular interactions toward other proteins in the solution. In Figure 12, symbols (a), (b) and (c) stand for experimental points for, respectively, pH values of 4.5, 7.0 and 10.0.

Note that for BSA adsorption onto nT-TiO<sub>2</sub> surface (case I), lower is the pH, higher is the  $I_{max}$  value (a, b, c decreasing order), while for BSA adsorption onto CaP.nT-TiO<sub>2</sub> and Sr.CaP.nT-TiO<sub>2</sub> (case II and III) the decreasing order of  $I_{max}$  values is b, a, c. In all cases, the lowest amount of BSA adsorbed is for the basic pH.

From each curves I(t) shown in Figure 12, we can estimate the slope that is related to the initial adsorption rate ( $\beta$  parameter =  $I_{max}/\tau$ ). Information obtained from Figure 12 are summarized in Table 2 where values of the parameter R and  $I_{max} = A_I + A_{II}$  and  $\beta$  are given for each adsorption case studied in this work.

Concerning  $\beta$  parameter, which is related to the adsorption rate for very low coverage rates, we observe values that are quite similar, except perhaps lower values for the adsorption in basic solutions for basic type surfaces (CaP.nT-TiO<sub>2</sub> and Sr.CaP.nT-TiO<sub>2</sub>) and a maximum value for pH = 7.0 on the Sr.CaP.nT-TiO<sub>2</sub> surface. Concerning  $I_{max}$ , we always notice a higher value, regardless of the nature of the surface, for pH 4.5 and 7.0 compared to basic pH 10.0.

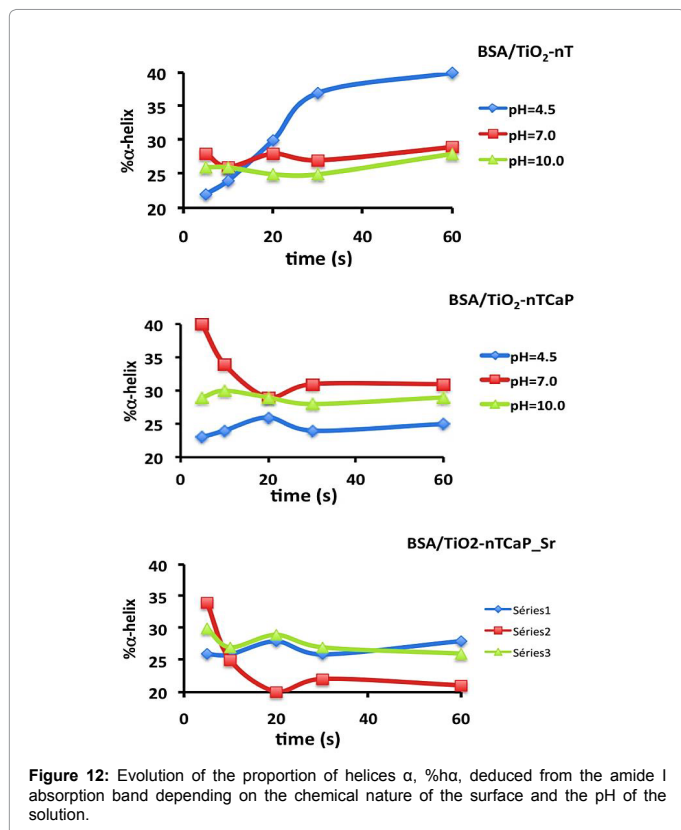
For pH 7.0, a noticeable increase of  $I_{max}$  is observed for functionalized surfaces with deposits of CaP and Sr.CaP, this increase being maximal for Sr.CaP.nT-TiO<sub>2</sub> surface.

In all cases we note that saturation is obtained very quickly (few minutes). Actually, similar results were obtained in similar conditions by Zeng et al. [22] who indicated the increase of BSA adsorption according to time particularly at the first several minutes. At about 5 min, the amounts of BSA adsorbed on all surfaces were close to the saturation values.

Note that in most cases, the value of R is relatively low ( $\approx 1$ ) except for the case of adsorption in a neutral pH for the Sr.CaP.nT-TiO<sub>2</sub> surfaces ( $R = 2.12$ ). From the above discussion, this would mean that BSA is adsorbed onto the surface with a high proportion of helices  $\alpha$  parallel to the sample surface, except for the Sr.CaP.nT-TiO<sub>2</sub> surface where BSA seems to keep its N form shape (end on adsorption). This high R value is in agreement with a greater  $I_{max}$  value as a more dense and compact protein layer must be formed at saturation coverage.

These results suggest a strong adsorption of this soft protein that can lead to modification of the tertiary and /or secondary structure of BSA in most if the case studied in this work. In the other case mentioned above, the R value is very close to that of a globular protein adsorption, without important deformation of the form N of BSA (value between 2.3 and 3.0). Note that these observations from Table 2 concern the final adsorption state (surface saturation). From Amide I band structure, we found significant changes in the amide band structure based on the coverage, and this depends on the chemical nature of the surface and the pH.

To follow the evolution of the amide I band for different pH values for adsorption on the different functionalized surfaces studied in this work, we have calculated the proportion of helices  $\alpha$  (% $\alpha$ ) in the mass of the amide I band (component at 1650 cm<sup>-1</sup>) and reported their evolution according to the deposition time. While the R parameter gives us information on the tertiary structure and/or about the orientation of the molecule with respect to the surface, % $\alpha$  parameter is linked to secondary structure modifications [54,57]. In each case, we observed that the decrease of % $\alpha$  is correlated with an increase of the peak corresponding to random coil (1636 cm<sup>-1</sup>). From Figure 12 we can



	nT-TiO <sub>2</sub>			CaP.nT-TiO <sub>2</sub>			Sr.CaP.nT-TiO <sub>2</sub>		
	4.5	7.0	10.0	4.5	7.0	10.0	4.5	7.0	10.0
A <sub>1</sub> +A <sub>11</sub>	0.20	0.14	0.11	0.23	0.31	0.17	0.23	0.57	0.11
A <sub>1</sub> /A <sub>1</sub> +A <sub>11</sub>	0.44	0.50	0.54	0.45	0.37	0.42	0.48	0.68	0.48
R	0.78	1.00	1.22	0.82	0.59	0.72	0.92	2.12	0.95
Δβ(s <sup>-1</sup> )	0.020	0.020	0.019	0.019	0.017	0.015	0.021	0.025	0.007

Table 2: Summary of R and β values for the different kinetics (ΔR = 0.05 and Δβ= 0.002).

observe that when adsorption takes place onto the nT-TiO<sub>2</sub> surface, %ha do not vary with BSA coverage (cerca 25-30%) for pH = 7.0 and pH = 10.0, while this parameter increases monotonously (20% to 40%) for pH = 4.5. Evolution of %ha with coverage and pH is quite different for the two basic surfaces CaP.nT-TiO<sub>2</sub> and Sr.CaP.nT-TiO<sub>2</sub>. For pH = 7.0, %ha started with a high value for low coverage then decreases to the minimum (about 20 s) before reaching a plateau. These observations reveal that BSA conformation evolves during the adsorption process depending on the surface acid-base properties and the pH.

**Discussion:** To explain the influence of surface chemistry and pH on the adsorbed BSA structure and conformation through the evolution of %ha and  $I_{max}$  and R, one have to remember that the solid surface and BSA have local charges that depend on the pH of aqueous medium where the adsorption occurs. For BSA, the ionization of different groups gives a global charge (electron charge unit) of +25, -10 and -70, respectively for pH = 4.5, 7.0, and 10.0. Note that each of the charges of side groups of amino acids is associated with a counter-ion, which results in the existence of a dipole rather than a locally isolated charge. This distribution of the dipole on the molecular surface is of course linked to the secondary and tertiary structure of BSA. Concerning the surface charges of the nanostructured nT-TiO<sub>2</sub> studied in this work, if we assume a PZC ≈ 3.0-4.0, the surface charge is nearly neutral for pH = 4.5 and globally negative for pH 7.0 and pH 10.0. In the case of the two others basic surfaces, CaP.nT-TiO<sub>2</sub> and Sr.CaP.nT-TiO<sub>2</sub> they are globally positively charged for pH = 4.5 and pH = 7.0 and neutral at pH = 10.0.

In general, Table 2 reveals R values near unity (except pH = 7.0 for Sr.CaP.nT-TiO<sub>2</sub>) meaning a strong tertiary structure modification, BSA molecule leaving its liquid state N form shape to get a more flat and extended shape in the adsorbed state. This tertiary structure modification is accompanied with a helix α denaturation for most cases studied here. We always have a lower %ha in the adsorbed state than in the liquid state (55-67%). Nevertheless, we observe a particular non constant evolution of %ha with BSA coverage in three cases; pH = 4.5 for nT-TiO<sub>2</sub> surface, pH = 7.0 for the two basic surfaces CaP.nT-TiO<sub>2</sub> and Sr.CaP.nT-TiO<sub>2</sub>. In the first case, BSA charge is positive with a global charge near +25 e. For the nT-TiO<sub>2</sub> surface, the net charge is negative and we expect strong electrostatic interactions between BSA and the TiO<sub>2</sub> nanotubes. These interactions are of course lower for pH = 7.0 and pH = 10.0, agreeing with a lower  $I_{max}$  value for these cases. R value is lower than 2.3, indicating that BSA is mostly adsorbed flat onto the surface in an unfolded form. The unfolding of BSA N form is a result of the accommodation of these electrostatic interactions with the tube edges.

The evolution of %ha with coverage indicates that when the adsorbed proteins get closer from each other in the adsorbed state, molecule-molecule interactions get more effective than molecule-surface interactions, leading to a secondary %ha structure recovery. So, this particular evolution of %ha with coverage for pH = 4.5 could be simply understand as a balance of electrostatic interactions between BSA and surface and BSA in its adsorbed state. Remark a lower  $I_{max}$

value for pH = 7.0 and pH = 10.0 that reveal a lower adsorbed molecules density, in accordance with lower intermolecular interactions in the adsorbed state, preventing their influence on the layer reorganization as depicted for pH = 4.5.

For CaP.nT-TiO<sub>2</sub> surface, photoemission allowed us to estimate a formula of the type Ca<sub>4</sub>(HPO<sub>4</sub>)<sub>3</sub>OH<sub>2</sub>, which indicates that at acid pH, the surface is composed of H<sub>2</sub>PO<sub>4</sub><sup>-</sup> groups. In the case of surfaces modified with Sr, a compound of the type Ca<sub>1-x</sub>Sr<sub>x</sub>(HPO<sub>4</sub>) have been evidenced, for which the same type of phosphate groups is expected for acidic pH. At acidic pH, BSA is positively charged and the coated basic surfaces are globally also positively charged. At neutral pH, BSA is nearly neutral (slightly negatively charged) and the coated basic surfaces are globally positively charged. At pH = 10.0, BSA is nearly negatively charged while the coated basic surfaces are nearly neutral.

The evolution of %ha for CaP.nT-TiO<sub>2</sub> and Sr.CaP.nT-TiO<sub>2</sub> surfaces suggests a similar behavior of BSA structure during the adsorption on these two surfaces at all pH. For these two basic surfaces, at pH = 7.0, the pH of the solution is close to the pKa of H<sub>2</sub>PO<sub>4</sub><sup>-</sup>/HPO<sub>4</sub><sup>2-</sup> couple and the surface must be composed of an equal surface density of groups H<sub>2</sub>PO<sub>4</sub><sup>-</sup> and HPO<sub>4</sub><sup>2-</sup>. For these basic surfaces immersed in a neutral solution, the parameter %ha is high (35-40%) for low coverage θ and decreases until 20.0 s of immersion before stabilization at a value of around 20%. This behavior is opposite to that observed for nT-TiO<sub>2</sub> case for a pH of 4.5. The diminution of %ha can be associated with a cooperative effect between the phosphate desorption (evidenced in IR spectra with the negative absorption band near 1100 cm<sup>-1</sup>) and the helices α denaturation. Phosphate desorption leads to surface Ca<sup>2+</sup> ions that were previously masked, as they were involved in a chemical bond with HPO<sub>4</sub><sup>2-</sup>. Thus, attractive interaction (anchor points) between Ca<sup>2+</sup> centers and some helices α could lead to secondary structure denaturation that increases with coverage as phosphate ions are released and %ha decrease with BSA coverage. As we do not observed this trend for pH = 10.0, where BSA is mostly negatively charged, we propose that it is the released phosphate ions that interacting with positive charge of BSA that are responsible for the helix α secondary structure denaturation rather than some negative BSA sites bonding with positive surface centers. When BSA is positively (pH = 4.5) or negatively (pH = 10) charged, %ha is low and nearly constant with BSA coverage, meaning that tertiary and secondary changes are more difficult in that cases, perhaps due to a greater protein shape stabilization due to electrostatic intramolecular interactions.

## Conclusion

Titanium surface nanostructuring (nT-TiO<sub>2</sub>) allows the creation of new surface sites with specific reactivity and are considered as preferential adsorption site for CaP as revealed by SEM. Pulsed electrodeposition was used to realize such a localized functionalization of titanium surface. Sr doped CaP coatings have also been deposited for different Sr concentrations in solution. Chemical composition of the adsorbed thin films has been observed by XPS and IR spectroscopies. Both IR and XPS spectra have clearly shown that the addition of Sr into the CaP layer favor Ca<sub>1-x</sub>Sr<sub>x</sub>HPO<sub>4</sub> compound similar to DCPA or

DCPD, while the pure CaP coating looks like an amorphous apatite-like compound ( $\alpha$ -ACP). Thus, applying pulsed electrodeposition enabled us to obtain a powerful chemical functionalization of nanostructured titanium surface with bioactive compound that is anchored on the nanotube edges which are considered as the most reactive nucleation sites on the (nT-TiO<sub>2</sub>) surface.

The ability of such functionalized surfaces to react with biological medium has been evaluated through BSA adsorption which was performed at different pH on blank nanotubes (nT-TiO<sub>2</sub>), nanotubes coated with CaP (CaP.nT-TiO<sub>2</sub>) and nanotubes coated with Sr doped CaP (Sr.CaP.nT-TiO<sub>2</sub>) in order to evaluate the influence of the chemical nature of the surface on protein adsorption process. Using IR spectra as a function of the quantity of the BSA adsorbed by the surface (amide band structure and area), we have found that BSA adsorption depends strongly on the physico-chemical characteristics of both surface and solution. For Sr doped CaP coatings, BSA seem to keep a non-denatured structure at neutral pH. This is an encouraging fact as in these conditions adsorbed proteins should keep their activity. As the local pH tends to get acidic after implantation, a next challenge would be to stabilize the pH medium near the implant surface to prevent proteins denaturation.

The observations obtained in this work can be used to design a functionalization of implant surface in order to favor the cellular adhesion and colonization. The evaluation of protein adsorption and its conformation as well as the protein-protein interactions may offer an opportunity to understand its interactions with adhering cells during the first steps of cellular colonization.

## References

- Takebe J, Itoh S, Okada J, Ishibashi K (2000) Anodic oxidation and hydrothermal treatment of titanium results in a surface that causes increased attachment and altered cytoskeletal morphology of rat bone marrow stromal cells in vitro. *J Biomed Mater Res* 51: 398-407.
- Zhu X, Son DW, Ong JL, Kim K (2003) Characterization of hydrothermally treated anodic oxides containing Ca and P on titanium. *J Mater Sci Mater Med* 14: 629-634.
- Skripitz R, Aspenberg P (1998) Tensile bond between bone and titanium: a reappraisal of osseointegration. *Acta Orthop Scand* 69: 315-319.
- Sul YT, Byon ES, Jeong Y (2004) Biomechanical measurements of calcium-incorporated oxidized implants in rabbit bone: effect of calcium surface chemistry of a novel implant. *Clin Implant Dent Relat Res* 6: 101-110.
- Le Guéhennec L, Soueidan A, Layrolle P, Amouriq Y (2007) Surface treatments of titanium dental implants for rapid osseointegration. *Dent Mater* 23: 844-854.
- Hoyer P (1996) Formation of a Titanium Dioxide Nanotube Array. *Langmuir* 12: 1411-1413.
- Anil S, Anand PS, Alghamdi H, Jansen JA (2011) *Implant Dentistry - A Rapidly Evolving Practice*. Intech publisher.
- Gong D, Grimes CA, Varghese OK, Hu W, Singh RS, et al. (2001) Titanium oxide nanotube arrays prepared by anodic oxidation. *J Mater Res* 16: 3331-3334.
- Lakshmi BB, Dorhout PK, Martin CR (1997) Sol-Gel Template Synthesis of Semiconductor Nanostructures. *Chem Mater* 9: 857-862.
- Lee HC, Zhang LF, Lin JL, Chin YL, Sun TP (2013) Development of anodic titania nanotubes for application in high sensitivity amperometric glucose and uric acid biosensors. *Sensors (Basel)* 13: 14161-14174.
- Marie PJ, Garba MT, Hott M, Miravet L (1985) Effect of low doses of stable strontium on bone metabolism in rats. *Miner Electrolyte Metab* 11: 5-13.
- Maimoun L, Brennan TC, Badoud I, Dubois-Ferriere V, Rizzoli R, et al. (2010) Strontium ranelate improves implant osseointegration. *Bone* 46: 1436-1441.
- Heughebaert JC, Montel G (1982) Conversion of amorphous tricalcium phosphate into apatitic tricalcium phosphate. *Calcif Tissue Int* 34 Suppl 2: S103-108.
- Wang XX, Yan W, Hayakawa S, Tsuru K, Osaka A (2003) Apatite deposition on thermally and anodically oxidized titanium surfaces in a simulated body fluid. *Biomaterials* 24: 4631-4637.
- Roy P, Berger S, Schmuki P (2011) TiO<sub>2</sub> nanotubes: synthesis and applications. *Angew Chem Int Ed Engl* 50: 2904-2939.
- Kar A, Raja KS, Misra M (2006) Electrodeposition of hydroxyapatite onto nanotubular TiO<sub>2</sub> for implant applications. *Surf Coat Tech* 201: 3723-3731.
- Zhu X, Chen J, Scheideler L, Reichl R, Geis-Gerstorfer J (2004) Effects of topography and composition of titanium surface oxides on osteoblast responses. *Biomaterials* 25: 4087-4103.
- Bernards MT, Qin C, Jiang S (2008) MC<sub>3</sub>T<sub>3</sub>-E<sub>1</sub> cell adhesion to hydroxyapatite with adsorbed bone sialoprotein, bone osteopontin, and bovine serum albumin. *Colloids Surf B Biointerfaces* 64: 236-247.
- Wen HB, de Wijn JR, van Blitterswijk CA, de Groot K (1999) Incorporation of bovine serum albumin in calcium phosphate coating on titanium. *J Biomed Mater Res* 46: 245-252.
- Ishida K, Yamaguchi M (2004) Role of Albumin in Osteoblastic Cells: Enhancement of Cell Proliferation and Suppression of Alkaline Phosphatase Activity. *International Journal of Molecular Medicine* 14: 1077-1081.
- Park JH, Lee YK, Kim KM, Kim KN (2005) Transformation of Electrodeposited Calcium Phosphate Coatings in Simulated Body Fluid and in Culture Medium. *Engineering Materials* 284-286: 473-476.
- Zeng H, Chittur KK, Laceyfield WR (1999) Analysis of bovine serum albumin adsorption on calcium phosphate and titanium surfaces. *Biomaterials* 20: 377-384.
- Kosmulski M (2009) *Surface charging and points of zero charge*. CRC Press, Taylor and Francis Group.
- Bavykin DV, Milsom EV, Marken F, Kim DH, Marsh DH, et al. (2005) A novel cation-binding TiO<sub>2</sub> nanotube substrate for electro-catalysis and bioelectro-catalysis. *Electrochemistry Communications* 7: 1050-1058.
- Kosmulski M (2001) *Chemical Properties of Material Surfaces*. Marcel Dekker Inc.
- Krimm S, Bandekar J (1986) Vibrational spectroscopy and conformation of peptides, polypeptides, and proteins. *Adv Protein Chem* 38: 181-364.
- Fu K, Griebenow K, Hsieh L, Klibanov AM, Langer R (1999) FTIR characterization of the secondary structure of proteins encapsulated within PLGA microspheres. *J Control Release* 58: 357-366.
- Mor GK, Varghese OK, Paulose M, Mukherjee N, Grimes CA (2003) Fabrication of tapered, conical-shaped Titania nanotubes. *J Mater Res* 18: 2588-2593.
- Cai Q, Paulose M, Varghes OK, Grimes CA (2005) The Effect of Electrolyte Composition on the Fabrication of Self-Organized Titanium Oxide Nanotube Arrays by Anodic Oxidation. *J Mater Res* (2005) 20: 230-236.
- Mor GK, Shankar K, Paulose M, Varghese OK, Grimes CA (2005) Enhanced photocleavage of water using titania nanotube arrays. *Nano Lett* 5: 191-195.
- Mor GK, Carvalho MA, Varghese OK, Pishko MV, Grimes CA (2004) A room-temperature TiO<sub>2</sub>-nanotube hydrogen sensor able to self-clean photoactively from environmental contamination. *J Mater Res* 19: 628-634.
- Park JH, Lee YK, Kim KM, Kim KN (2005) Bioactive calcium phosphate coating prepared on H<sub>2</sub>O<sub>2</sub>-treated titanium substrate by electrodeposition. *Surf Coat Tech* 195: 252-257.
- Narayanan R, Seshadri SK, Kwon TY, Kim KH (2008) Calcium phosphate-based coatings on titanium and its alloys. *J Biomed Mater Res B Appl Biomater* 85: 279-299.
- Wagner CD (1990) *Practical Surface Analysis* (2<sup>nd</sup> Edn). J Wiley and Sons.
- Arai Y, Sparks DL (2001) ATR-FTIR Spectroscopic Investigation on Phosphate Adsorption Mechanisms at the Ferrihydrite-Water Interface. *J Colloid Interf Sci* 241: 317-326.
- Lu HB, Campbell CT, Graham DJ, Rather BD (2000) Surface characterization of hydroxyapatite and related calcium phosphates by XPS and TOF-SIMS. *Anal Chem* 72: 2886-2894.
- Gadaleta SJ, Gericke A, Boskey AL, Mendelsohn R (1998) Two-dimensional infrared correlation spectroscopy of synthetic and biological apatites. *Biospectroscopy* 2: 353-364.

38. Ntais S, Dracopoulos V, Siokou A (2004) TiCl<sub>4</sub> (THF)<sub>2</sub> impregnation on a flat SiO<sub>2</sub>/Si (100) and on polycrystalline Au foil: determination of surface species using XPS. *J Mol Catal A Chem* 220: 199-205.
39. Müller L, Conforto E, Caillard D, Müller FA (2007) Biomimetic apatite coatings—carbonate substitution and preferred growth orientation. *Biomol Eng* 24: 462-466.
40. Kunze J, Müller L, Macak JM, Greil P, Schmuki P, et al. (2008) Time-dependent growth of biomimetic apatite on anodic TiO<sub>2</sub> nanotubes. *Electrochimica Acta* 53: 6995-7003.
41. Stranick MA, Root MJ (1991) Influence of strontium on monofluorophosphate uptake by hydroxyapatite XPS characterization of the hydroxyapatite surface. *Colloid and Surfaces* 55: 137-147.
42. Combes C, Rey C (2010) Amorphous calcium phosphates: synthesis, properties and uses in biomaterials. *Acta Biomater* 6: 3362-3378.
43. Christoffersen J, Christoffersen MR, Kibalczyk W, Andersen FA (1989) A contribution to the understanding of the formation of calcium phosphates. *J Cryst Growth* 94: 767-777.
44. Chahair H, Heughebaert JC, Heughebaert M (1995) Precipitation of stoichiometric apatitic tricalcium phosphate prepared by a continuous process. *J Mater Chem* 5: 895-899.
45. Dorozhkin SV, Epple M (2002) Biological and medical significance of calcium phosphates. *Angew Chem Int Ed Engl* 41: 3130-3146.
46. Gomes S, Renaudin G, Jallot E, Nedelec JM (2009) Structural characterization and biological fluid interaction of Sol-Gel-derived Mg-substituted biphasic calcium phosphate ceramics. *App Mater Int* 1: 505-513.
47. Chusuei CC, Goodman DW, Stipdonk MJV, Justes DR, Schweikert EA (1999) Calcium Phosphate Phase Identification Using XPS and Time-of-Flight Cluster SIMS. *Anal Chem* 71: 149-153.
48. Casciani FS, Condrate RA (1980) Sr Proc Int Cong Phosphorus Comp: 175-190.
49. Suguna K, Sekar C (2011) Role of Strontium on the Crystallization of Calcium Hydrogen Phosphate Dihydrate. *J Miner Mat Character Eng* 10: 625-636.
50. Mevellec JY, Quillard S, Deniard P, Mekmene O, Gaucheron F, et al. (2013) Polarized infrared reflectance spectra of brushite (CaHPO<sub>4</sub>•2H<sub>2</sub>O) crystal investigation of the phosphate stretching modes. *Spectrochim Acta A* 111: 7-13.
51. Wang L, Nancollas GH (2008) Calcium orthophosphates: crystallization and dissolution. *Chem Rev* 108: 4628-4669.
52. Farlay D, Panczer G, Rey C, Delmas PD, Boivin G (2010) Mineral maturity and crystallinity index are distinct characteristics of bone mineral. *J Bone Miner Metab* 28: 433-445.
53. Shemesh A (1990) Crystallinity and diagenesis of sedimentary apatites. *Geochimica et Cosmochimica Acta* 54: 2433-2438.
54. Rothschild KJ, Sanches R, Hsiao TL, Clark NA (1980) A spectroscopic study of rhodopsin alpha-helix orientation. *Biophys J* 31: 53-64.
55. Gallardo FI, Webb JL (2010) Tethering Hydrophobic Peptides to Functionalized Self-Assembled Monolayers on Gold through Two Chemical Linkers Using the Huisgen Cycloaddition. *Langmuir* 26: 18959-18966.
56. Zhu XD, Fan HS, Xiao YM, Li DX, Zhang HJ, et al. (2009) Effect of surface structure on protein adsorption to biphasic calcium-phosphate ceramics in vitro and in vivo. *Acta Biomater* 5: 1311-1318.
57. Wu H, Fan Y, Sheng J, Sui SF (1993) Induction of changes in the secondary structure of globular proteins by a hydrophobic surface. *Eur Biophys J* 22: 201-205.